# Hierarchically Porous Polymer Coatings for Highly Efficient Passive Daytime Radiative Cooling

**Authors:** J. Mandal[1], Y. Fu[1], A. Overvig[1], M. Jia[2], K. Sun[1], N. Shi[1], H. Zhou[3], X. Xiao[3], N. Yu[1]*, Y. Yang[1]*

**Affiliations:**

[1]Department of Applied Physics and Applied Mathematics, Columbia University, New York-10027, USA.

[2] Department of Mechanical Engineering, Columbia University, New York-10027, USA

[3] Advanced Photon Source, Argonne National Laboratory, Lemony, IL 60439, USA

*Correspondence to: Email: yy2664@columbia.edu (Y. Y.); ny2214@columbia.edu (N. Y.)

**One Sentence Summary:** A radiative cooling performance under sunlight superior to state-of-the-art designs, obtained with a paint-like convenience.

**Abstract:** Passive daytime radiative cooling (PDRC) involves spontaneously cooling a surface by reflecting sunlight and radiating heat to the cold outer space. Current PDRC designs are promising alternatives to electrical cooling, but are either inefficient or have limited applicability. We present a simple, inexpensive and scalable phase-inversion-based method for fabricating hierarchically porous poly(vinylidene fluoride-co-hexafluoropropene) $(P(VdF-HFP)_{HP})$ coatings with excellent PDRC capability. High, substrate-independent hemispherical solar reflectances $(0.96 \pm 0.03)$ and long-wave infrared (LWIR) emittances $(0.97 \pm 0.02)$ allow for sub-ambient temperature drops of ~6°C and cooling powers of ~96 W m$^{-2}$ under solar intensities of 890 and 750 W m$^{-2}$ respectively. The performance equals or surpasses those of state-of-the-art PDRC designs, while the technique offers a paint-like simplicity.

**Main Text:**

Cooling human-made structures, such as buildings, is a widespread necessity faced by humans today (*1*). However, compression-based cooling systems that are prevalently used (e.g. air conditioners) consume significant amount of energy, have a net heating effect, require ready access

to electricity, and often require coolants that are ozone-depleting or have a strong greenhouse effect
(*2, 3*). Therefore, inexpensive, eco-friendly approaches with net cooling capability are desirable
for reducing energy costs, operation time, and associated ozone-depleting and $CO_2$ emissions from
traditional cooling systems, or provide relief where electrical cooling is not available. One
alternative to energy-intensive cooling methods is passive daytime radiative cooling (PDRC) – a
phenomenon where a surface spontaneously cools by reflecting sunlight (wavelengths ($\lambda$) ~0.3-
2.5 μm) and radiating heat to the cold outer space through the atmosphere's long-wave infrared
(LWIR) transmission window ($\lambda \sim$ 8-13 μm). PDRC is most effective if a surface has a high,
hemispherical solar reflectance ($\bar{R}_{solar}$) that minimizes solar heat gain, and a high, hemispherical,
LWIR thermal emittance ($\bar{\epsilon}_{LWIR}$) that maximizes radiative heat loss (*4*). If $\bar{R}_{solar}$ and $\bar{\epsilon}_{LWIR}$ are
sufficiently high, a net radiative heat loss can occur, even under sunlight. The passive nature of
this effect makes PDRC highly appealing, as cooling occurs without the need for electricity,
refrigerants, or mechanical pumps that require maintenance.

Research in recent decades has yielded a variety of PDRC designs comprising sophisticated
emissive coatings such as photonic structures, dielectrics, polymers and polymer-dielectric
composites on metal mirrors (*5-11*). Although efficient, these designs are costly and susceptible to
corrosion. Furthermore, unlike paints, they are pre-fabricated, and cannot be directly applied to
existing roofs or walls, which have various compositions, textures and geometries (*7, 9, 10*).
Therefore, cool-roof paints (CRPs), which combine a modest optical performance with easy
applicability and inexpensiveness, remain the benchmark for PDRC (*12-15*). However, CRPs,
which comprise dielectric pigments (e.g. titania and zinc oxide) embedded in a polymer matrix,
have a low solar reflectance (typically ~0.85) due to the pigments' ultraviolet (UV) absorptance
and the low near-to-short wavelength infrared (NIR-to-SWIR, $\lambda$ ~0.7-2.5 μm) reflectance (*13*). We

realized that replacing the pigments in CRPs with light-scattering air voids can not only eliminate this problem and increase the optical performance to state-of-the-art levels, but also avoid the material, processing and environmental costs associated with pigments (*14, 16*). Inspired by this idea, we report a simple, scalable and inexpensive phase-inversion-based process for fabricating hierarchically porous polymer coatings that exhibit excellent $\bar{R}_{solar}$ and $\bar{\epsilon}_{LWIR}$. Specifically, we achieved substrate-independent hemispherical $\bar{R}_{solar} = 0.96 \pm 0.03$ and $\bar{\epsilon}_{LWIR} = 0.97 \pm 0.02$ with hierarchically porous poly(vinylidene fluoride-co-hexafluoropropene) (P(VdF-HFP)$_{HP}$). The values result in a superb PDRC capability, exemplified by a sub-ambient cooling of ~6°C and an average cooling power of ~96 W m$^{-2}$ under solar intensities of 890 and 750 W m$^{-2}$, respectively. The performance is on par with or exceeds those in previous reports (*7, 9, 10*). Because the fabrication technique is room-temperature and solution-based, the porous polymer coatings can be applied by conventional approaches like painting and spraying to diverse surfaces like plastics, metal and wood. Moreover, it can incorporate dyes to achieve a desirable balance between color and cooling performance. The performance of the coatings and the paint-like convenience of the technique make it promising as a viable way to achieve high-performance PDRC.

Our phase-inversion-based method for making hierarchically porous polymers starts with the preparation of a precursor solution of P(VdF-HFP) (polymer) and water (non-solvent) in acetone (solvent) (Fig. 1A). We apply a film onto a substrate and dry it in air. The rapid evaporation of the volatile acetone causes the P(VdF-HFP) to phase-separate from the water, which forms micro- and nanodroplets. The P(VdF-HFP)$_{HP}$ coating is formed (Fig. 1A-B) after the water evaporates. The micro- and nano-pores in the coating efficiently backscatter sunlight and enhance thermal emittance (Fig. 1C). Consequently, P(VdF-HFP)$_{HP}$ films with ~50% porosity and thickness $\gtrsim 300$ μm have an exceptional, substrate-independent hemispherical $\bar{R}_{solar}$ of 0.96 and $\bar{\epsilon}_{LWIR}$ of 0.97

(Fig. 1 D to F). At thicknesses $\gtrsim$ 500 μm, $\bar{R}_{solar} \gtrsim 0.98$ is achieved (Fig. S2, S15). The high $\bar{R}_{solar}(\theta)$ ensures excellent reflection of sunlight from all incidences (Fig. 1E) and eliminates the need for silver reflectors used in previous designs (*7, 9, 10*), while the high $\bar{\epsilon}_{LWIR}(\theta)$ leads to a hemispherical $\bar{\epsilon}_{LWIR}$ that is > 10% higher than previously reported values (Fig. 1F) (*7, 9*). The precursor's paint-like applicability makes P(VdF-HFP)$_{HP}$ attractive for practical use.

5
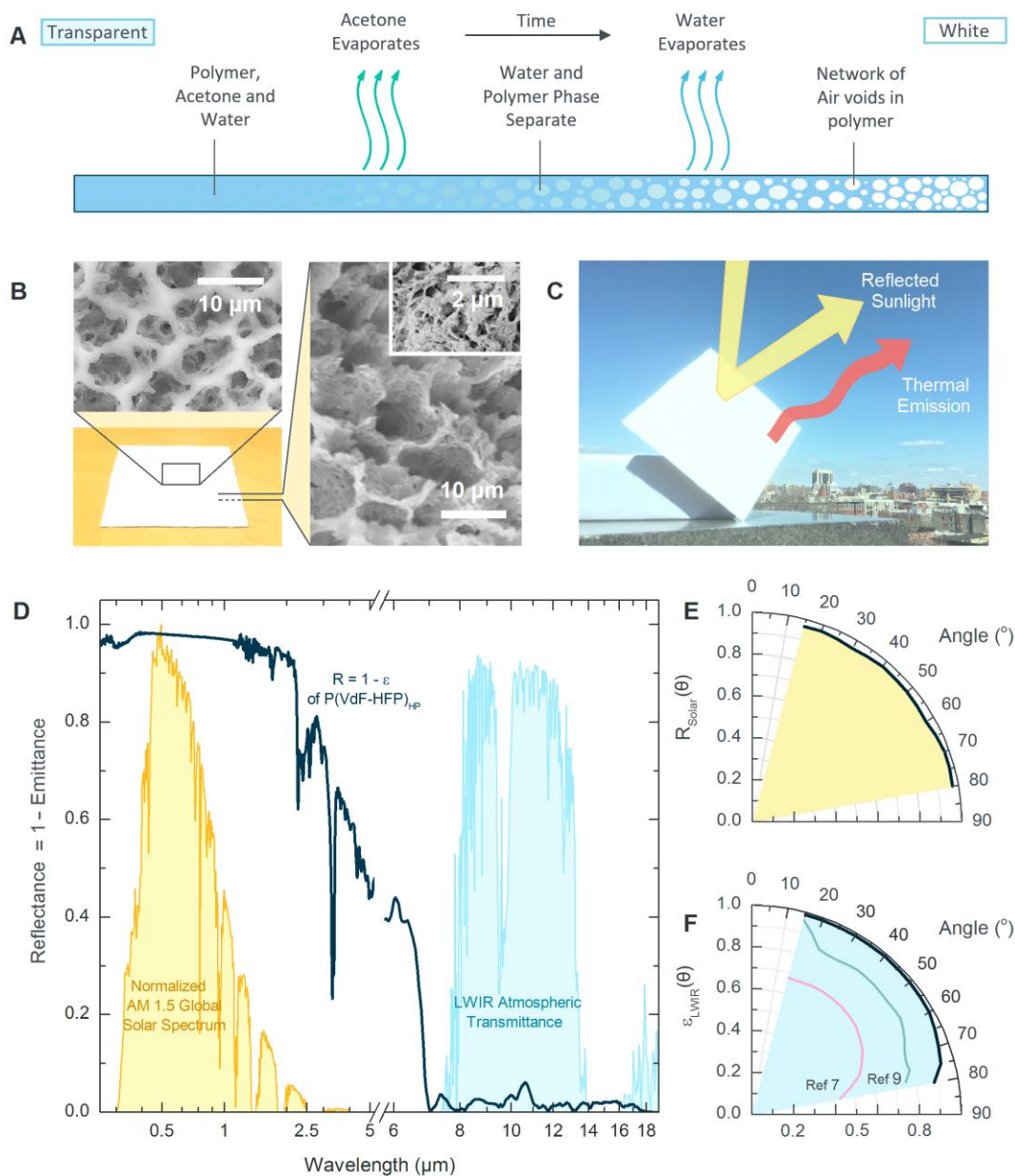
**Figure 1.** The formation and optical properties of P(VdF-HFP)$_{HP}$. (**A**) Schematic of the phase inversion process, showing the formation of a hierarchically porous polymer coating from a solution of acetone (solvent), water (non-solvent) and P(VdF-HFP) (polymer). (**B**) Micrographs showing top and cross-section views of P(VdF-HFP)$_{HP}$. Inset shows the nanoporous features. (**C**) Photograph superimposed with schematics to show that high $\bar{R}_{solar}$ and $\bar{\epsilon}_{LWIR}$ enable a net radiative loss and PDRC. (**D**) Spectral

reflectance ($R(\lambda) = 1 - \epsilon(\lambda)$) of a 300 μm thick P(VdF-HFP)$_{HP}$ coating presented against normalized ASTM G173 Global solar spectrum and the LWIR atmospheric transparency window. $\bar{R}_{solar}$ (0.96) and $\bar{\epsilon}_{LWIR}$ (0.97) are remarkably high, especially since they are achieved on a black selective solar absorber (Fig. S2) (*17*). (**E**) P(VdF-HFP)$_{HP}$'s high $\bar{R}_{solar}(\theta)$ and (**F**) $\bar{\epsilon}_{LWIR}(\theta)$ across angles result in excellent hemispherical $\bar{R}_{solar}$ and $\bar{\epsilon}_{LWIR}$.

P(VdF-HFP) (Fig. 2A) has ideal intrinsic electromagnetic properties for PDRC applications. Firstly, it has a negligible extinction coefficient across the solar wavelengths ($\lambda = 0.3\text{-}2.5$ μm) (Fig. 2B), unlike dielectric pigments of paints (Fig. S10) and silver, which both absorb UV light. This keeps solar heating to a minimum. Secondly, the polymer has multiple extinction peaks in the thermal wavelengths, including 14 in the LWIR window, which arise from the different vibrational modes of its molecular structure (Fig. 2B) (*18-20*). Consequently, P(VdF-HFP) efficiently radiates heat in the LWIR window, where peak blackbody emissions from terrestrial surfaces and a high atmospheric transmittance into space coincide.

When structured by the phase-inversion technique into a hierarchical form consisting of ~ 2-10 μm micropores partitioned by a nanoporous phase (Figs. 1B and S4), P(VdF-HFP) exhibits high $\bar{R}_{solar}$ and $\bar{\epsilon}_{LWIR}$. Pore size measurements indicate that the pore sizes are bimodally distributed, with broad distributions centered at ~ 0.2 μm and ~5.5 μm for the nano- and micropores respectively (Fig. 2C) (*4*). As corroborated by finite-difference time-domain simulations (*4*), the abundant micropores with sizes ~5 μm efficiently scatter sunlight of all wavelengths (Fig. 2D). This is further enhanced by the nanopores with sizes ~50-500 nm, which strongly scatter shorter, visible wavelengths (Fig. 2D). The simulations are also experimentally substantiated by diffuse transmission characterizations, which yield a photon mean free path ($l_f$) of ~ 6 μm for the blue wavelengths and ~ 10 μm for the NIR wavelengths (Fig. S3). In the absence of any intrinsic

absorption, this results in a high optical backscattering of sunlight and thus a matte, white appearance. Furthermore, the unoriented pores result in a high, diffuse $\bar{R}_{solar}(\theta)$ regardless of the angle of incidence (Fig. 1E). In the thermal wavelengths, the emittance is likely enhanced across the LWIR window by the broadening of the extinction peaks (Fig. 2B) due to impurities (e.g. moisture), polymer chain deformation and amorphousness in the nanoporous polymer (*21-23*). We attribute the high $\bar{\epsilon}_{LWIR}(\theta)$ for a wide, angular range (Fig. 1F) to the open, porous surface (Fig. 1B) and the effective medium behavior of the nanoporous P(VdF-HFP)$_{HP}$ coating at large wavelengths (*4*). A combination of these two features provides a gradual refractive index transition across polymer-air boundaries. Therefore, emitted radiation is not hindered at the surface and $\bar{\epsilon}_{LWIR}(\theta)$ is high regardless of the angle (Fig. 2 E-F).
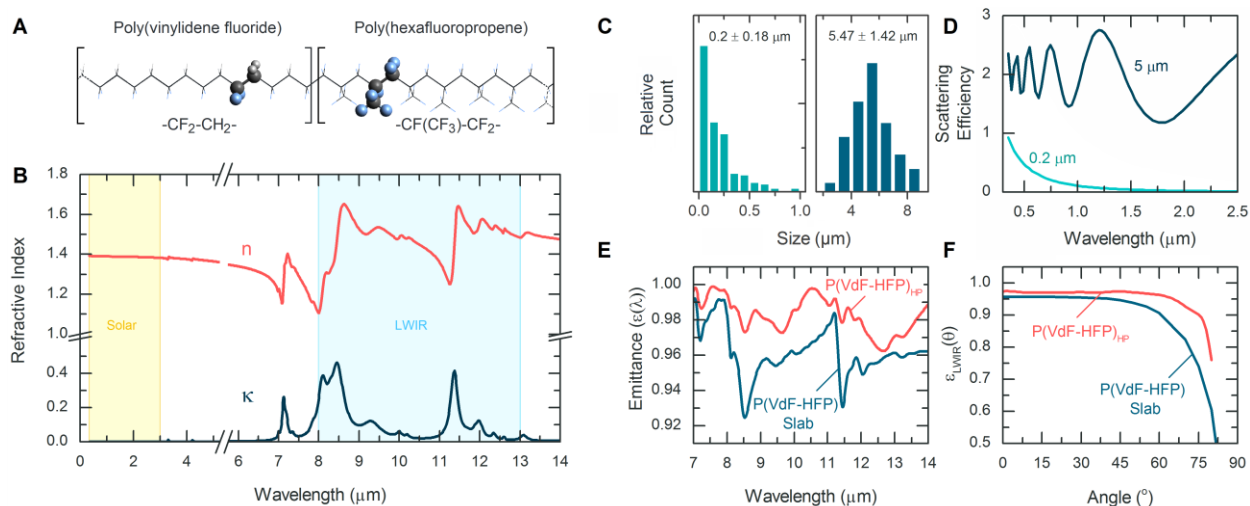


**Figure 2.** The optical properties of P(VdF-HFP)$_{HP}$. (**A**) A wireframe showing the structure of P(VdF-HFP), with the VdF and HFP repeating units shown. (**B**) Experimental complex spectral refractive index (n + iκ) of P(VdF-HFP), showing negligible absorptivity in the solar, and high emissivity in the LWIR wavelengths. The peaks in κ correspond to the vibrational modes of different molecular components (e.g. CF$_3$, CF$_2$, CF, C-C, CH$_2$, C-H, and carbon backbone) (*15-17*). (**C**) Size distributions of nano and micropores in P(VdF-

HFP)$_{HP}$, showing number-weighted mean pore sizes of ~ 0.2 μm for nanopores and ~5.5 μm for micropores. (**D**) Simulated scattering cross-section spectra of circular micro- and nano-voids in P(VdF-HFP)$_{HP}$. Voids of different sizes collectively scatter all solar wavelengths, resulting in a high $\bar{R}_{solar}$. (**E**) Spectral LWIR emittance and (**F**) $\bar{\epsilon}_{LWIR}(\theta)$ of P(VdF-HFP)$_{HP}$ compared to a solid PVDF slab of the same volume. As evident, the former has a higher spectral and angular emittance. Further details are provided in the Supplementary Information (*4*).

The high $\bar{R}_{solar}$ and $\bar{\epsilon}_{LWIR}$ allow P(VdF-HFP)$_{HP}$ coatings to achieve remarkable daytime sub-ambient cooling under widely different skies of Phoenix (USA), New York (USA) and Chattogram (Bangladesh) (Fig. 3). For instance, under a peak solar intensity $I_{solar}$ of ~890 W m$^{-2}$ and a clear sky with low humidity in Phoenix, P(VdF-HFP)$_{HP}$ coatings without any convection shields achieved a sub-ambient temperature drop (ΔT) of ~6°C. Promisingly, ΔT ~3°C was also observed in Chattogram, where fog and haze impeded radiative heat loss into the sky. P(VdF-HFP)$_{HP}$ coatings also attained remarkable cooling powers ($P_{cooling}$, *4*) of 96 W m$^{-2}$ and 83 W m$^{-2}$ in Phoenix and New York respectively. The values are consistent with theoretical calculations (Table S1), and indicate P(VdF-HFP)$_{HP}$'s potential to reduce air-conditioning costs of buildings. We cannot directly compare the performance to earlier results, as $P_{cooling}$ depends heavily on experimental design, geography, and meteorological variables (Table S2, *24-26*). Nevertheless, the high performance without convection shields in different climates indicate that P(VdF-HFP)$_{HP}$'s PDRC capability is better or on par with high-performance PDRC results in the literature (*7, 9, 10*).
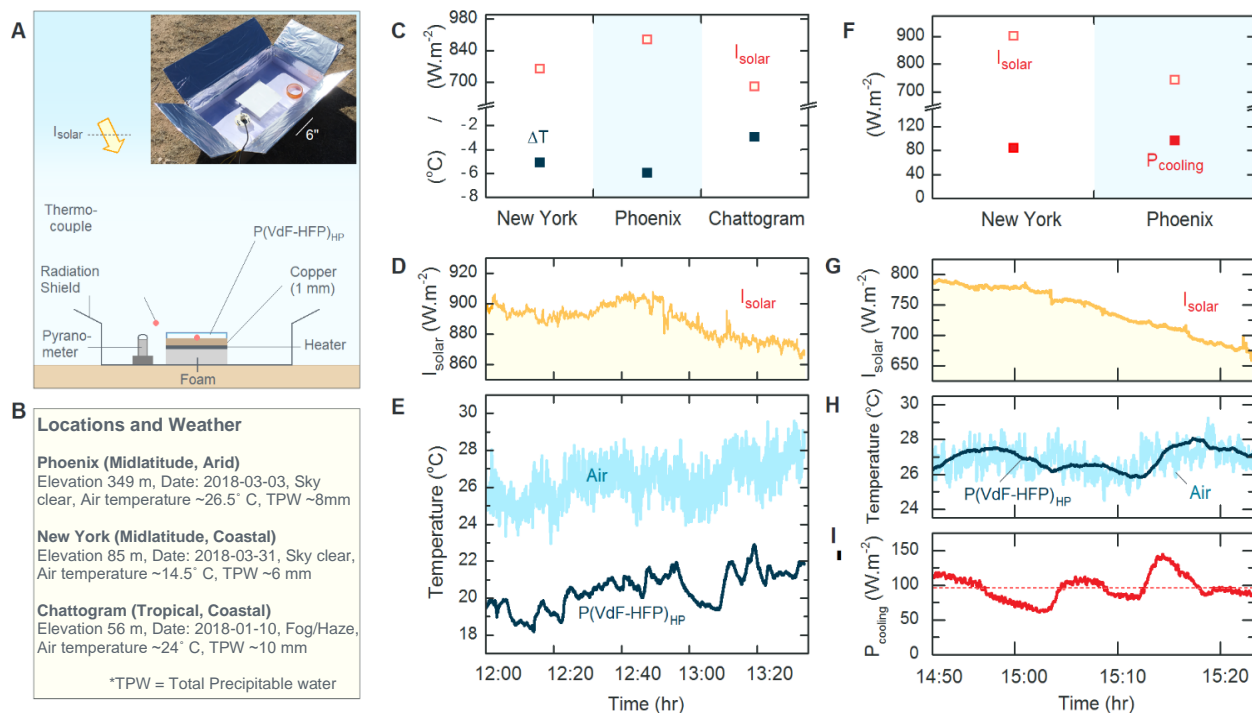
**Figure 3.** Passive daytime radiative cooling performance of P(VdF-HFP)$_{HP}$. (**A**) Schematic of the setup for testing performance under sunlight. (**B**) Topographic and meteorological information of the test locations. (**C**) Average solar intensity (I$_{solar}$) and sub-ambient temperature drops (ΔT) of P(VdF-HFP)$_{HP}$ coatings in New York, Phoenix and Chattogram. (**D**) Detailed I$_{solar}$ and (**E**) temperature data of the result for Phoenix in C. (**F**) I$_{solar}$ and cooling powers ($P_{cooling}$) of P(VdF-HFP)$_{HP}$ coatings measured in New York and Phoenix. (**G**) Detailed I$_{solar}$, (**H**) Temperature tracking and (**I**) $P_{cooling}$ data of the result for Phoenix in F. Dotted line in (I) indicates average $P_{cooling}$ over the duration of the experiment. Additional information is provided in the Supplementary Information (*4*).

The excellent optical performance of P(VdF-HFP)$_{HP}$ is complemented by a paint-like applicability, which is crucial for direct application on structures. We can paint, dip-coat, or spray P(VdF-HFP)$_{HP}$ onto diverse substrates like metal, plastics and wood (Fig. 4A-C). Furthermore, P(VdF-HFP)$_{HP}$ can also be made into strong, recyclable sheets (Fig. 4D, Figs. S12-13). We also conducted accelerated thermal aging and moisture testing that showed the durability of the coatings and sheets (Table S3). P(VdF-HFP) is intrinsically resistant to weathering, fouling and ultraviolet radiation

(*22, 27*). When made porous, it hydrophobically repels waterborne dirt (Fig. S14). During accelerated aging and monthlong outdoor exposure tests, these properties enabled P(VdF-HFP)$_{HP}$ to retain its optical performance at near-pristine levels (Table S3, Fig. S15). For instance, a monthlong outdoor exposure in New York City only changed $\bar{R}_{solar}/\bar{\epsilon}_{LWIR}$ from 0.94/0.93 to 0.93/0.93.
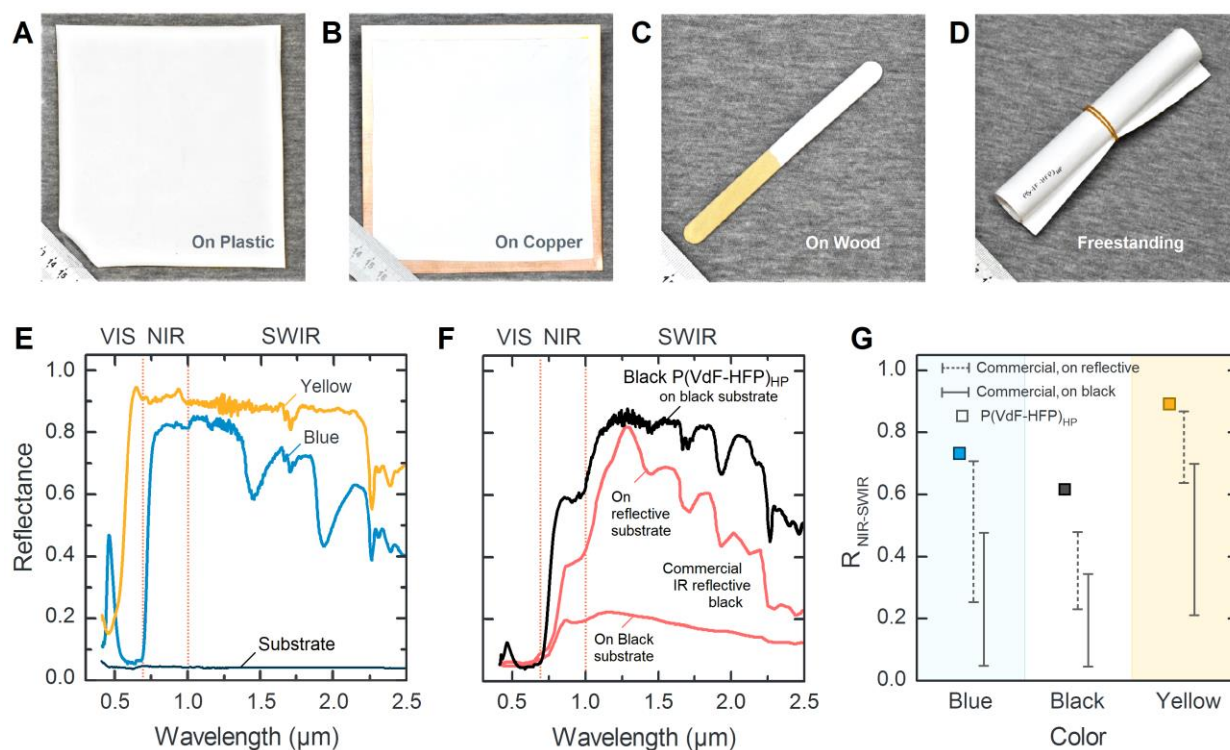


**Figure 4.** Versatility of P(VdF-HFP)$_{HP}$ coatings. P(VdF-HFP)$_{HP}$ can be (**A**) painted onto plastics (**B**) spray-coated on copper (**C**) dip-coated on wood and (**D**) made into strong, flexible and freestanding sheets for tarpaulin-like designs. (**E**) Spectral reflectances of ~350 μm thick blue and yellow P(VdF-HFP)$_{HP}$ coatings and (**F**) of a black P(VdF-HFP)$_{HP}$ coating compared to a commercial black pigment on reflective and black substrates. (**G**) Despite being on black substrates, their $\bar{R}_{NIR-SWIR}$ surpasses those of similarly colored 'IR-reflective' pigments (~25 μm thick films) on both black and reflective substrates.

An often-unstated but important practical requirement for PDRC coatings is compatibility with colors. To minimize solar heating, colored PDRC coatings should maximize the reflection of NIR-

to-SWIR wavelengths (0.7-2.5 µm), which contain ~51% of solar energy but are invisible to the human eye. However, paints typically have low reflectances ($\bar{R}_{NIR-SWIR}$) in the NIR-to-SWIR wavelengths (Fig. S10) (*13, 28*). In contrast, porous P(VdF-HFP)$_{HP}$ coatings containing blue, yellow, and black dyes and with thickness ~350 µm efficiently backscatter sunlight not absorbed by the dyes to yield correspondingly colored coatings with high $\bar{R}_{NIR-SWIR}$ of 0.73, 0.89 and 0.62 respectively (Figs. 4E-F). These values were measured with black substrates, but exceed reflectances of thin films (~25 µm) of similarly colored 'IR-reflective' pigments on reflective substrates (Figs. 4F-G), and of the same pigments on black substrates by a large margin (*28, 29*). Dyed P(VdF-HFP)$_{HP}$ coatings may thus address the longstanding problem of achieving PDRC with colored coatings, greatly widening their scope of use.

Finally, we note that the phase-inversion-based technique, shown here for P(VdF-HFP)$_{HP}$, is compatible with a wide variety of polymers. The method thus allows optically suitable polymers to be easily structured into PDRC coatings with other potential benefits. For instance, poly(methyl methacrylate) yields glossy coatings, ethyl cellulose provides biocompatibility and enables use of eco-friendly solvents, and polystyrene enables operation at temperatures > 200˚C (Fig. S16). The diverse possibilities makes the phase-inversion-based technique a viable pathway for making both generic and specialized PDRC coatings.

**References and Notes:**

1.  M. Burke, S. M. Hsiang, E. Miguel, Global non-linear effect of temperature on economic production. *Nature* **527**, 235 (2015).
2.  World Bank (2017). *Access to Electricity*. Retrieved from https://data.worldbank.org/indicator/EG.ELC.ACCS.RU.ZS.
3.  United States Environment Protection Agency (2018). *Phaseout of Ozone-Depleting Substances (ODS)*. Retrieved from https://www.epa.gov/ods-phaseout.
4.  Materials and methods are available in the Supplementary Information.

5.    T. S. Eriksson, S. J. Jiang, C. G. Granqvist, Surface coatings for radiative cooling applications: Silicon dioxide and silicon nitride made by reactive rf-sputtering. *Solar Energy Materials* **12**, 319-325 (1985).

6.    C. G. Granqvist, A. Hjortsberg, Surfaces for radiative cooling: Silicon monoxide films on aluminum. *Applied Physics Letters* **36**, 139-141 (1980).

7.    A. P. Raman, M. A. Anoma, L. Zhu, E. Rephaeli, S. Fan, Passive radiative cooling below ambient air temperature under direct sunlight. *Nature* **515**, 540-544 (2014).

8.    A. R. Gentle, G. B. Smith, Radiative Heat Pumping from the Earth Using Surface Phonon Resonant Nanoparticles. *Nano Letters* **10**, 373-379 (2010).

9.    A. R. Gentle, G. B. Smith, A Subambient Open Roof Surface under the Mid-summer Sun. *Advanced Science* **2(9)**, (2015).

10.   Y. Zhai *et al.*, Scalable-manufactured randomized glass-polymer hybrid metamaterial for daytime radiative cooling. *Science* **355**, 1062-1066 (2017).

11.   N. Yu, J. Mandal, A. C. Overvig, N. N. Shi. (The Trustees of Columbia University in the City of New York, 2016), chap. WO2016205717A1.

12.   C. S. Wojtysiak, J. W. Butler. (SkyCool Pty Ltd, 2009), chap. PCT/AU02/00695.

13.   J. Song *et al.*, The effects of particle size distribution on the optical properties of titanium dioxide rutile pigments and their applications in cool non-white coatings. *Solar Energy Materials and Solar Cells* **130**, 42-50 (2014).

14.   G. T. J. Bentley, *Introduction to Paint Chemistry*. (Springer Science, Bristol, UK, ed. 4, 1998).

15.   Cool Roof Rating Council. *Rated Products Directory.* Retrieved from https://coolroofs.org/directory.

16.   A. Al-Kattan *et al.*, Behavior of TiO2 Released from Nano-TiO2-Containing Paint and Comparison to Pristine Nano-TiO2. *Environmental Science & Technology* **48**, 6710-6718 (2014).

17.   J. Mandal *et al.*, Scalable, "Dip-and-Dry" Fabrication of a Wide-Angle Plasmonic Selective Absorber for High-Efficiency Solar–Thermal Energy Conversion. *Advanced Materials* **29**, 201702156 (2017).

18.   Y. Bormashenko, R. Pogreb, O. Stanevsky, E. Bormashenko, Vibrational spectrum of PVDF and its interpretation. *Polymer Testing* **23**, 791-796 (2004).

19.   M. Kobayashi, K. Tashiro, H. Tadokoro, Molecular Vibrations of Three Crystal Forms of Poly(vinylidene fluoride). *Macromolecules* **8**, 158-171 (1975).

20.   L. N. Sim, S. R. Majid, A. K. Arof, FTIR studies of PEMA/PVdF-HFP blend polymer electrolyte system incorporated with LiCF3SO3 salt. *Vibrational Spectroscopy* **58**, 57-66 (2012).

21.   H. Hagemann, R. G. Snyder, A. J. Peacock, L. Mandelkern, Quantitative infrared methods for the measurement of crystallinity and its temperature dependence: polyethylene. *Macromolecules* **22**, 3600-3606 (1989).

22.   Arkema (2017). *KYNAR® & KYNAR FLEX® PVDF Performance Characteristics and Data.* Retrieved from https://www.extrememterials-arkema.com/en/product-families/kynar-pvdf-family/download-performance-characteristics-data-brochure.

23.   R. S. Bretzlaff, R. P. Wool, Frequency shifting and asymmetry in infrared bands of stressed polymers. *Macromolecules* **16**, 1907-1917 (1983).

24.   T. S. Eriksson, C. G. Granqvist, Radiative cooling computed for model atmospheres. *Applied Optics* **21**, 4381-4388 (1982).

25. A. W. Harrison, M. R. Walton, Radiative cooling of TiO2 white paint. *Solar Energy* **20**, 185-188 (1978).

26. C. J. Chen, in *Physics of Solar Energy*. (John Wiley & Sons, Inc., Hoboken, 2011), pp. 77-104.

27. Arkema (2008). *New fluoropolymer latex technology for cool materials solutions across an expanded color space*. Retrieved from http://coolcolors.lbl.gov/assets/docs/PAC-2008-03-06/Arkema-slides.pdf.

28. BASF (2017) *Ultra-cool - The new heat reflective coatings from BASF*. Retrieved from http://www2.basf.us/pdfs/ULTRA-Cool.pdf. .

29. R. Levinson, P. Berdahl, H. Akbari, Solar spectral optical properties of pigments—Part II: survey of common colorants. *Solar Energy Materials and Solar Cells* **89**, 351-389 (2005).

**availability:** All data are available in the manuscript or in the supplementary materials. Information requests should be directed to the corresponding authors.


**Supplementary Materials:**

5       Materials and Methods

Supplementary Text.

Figures S1 to S16.

Tables S1 to S3.